Supporting Information

Breaking the Scaling Relationship for Oxygen Reduction via Amino-molecule-interface-mediated Metallene Electrocatalysts

Shuya Xu, Yunyi Zhang, Yukun Peng, Jiawei Ke, Xueheng Liu, Chenglin Yan, Lifang Zhang, Tongfei Li,* and Tao Qian*

S.s Xu, Y. Zhang, Y. Peng, J. Ke, X. Liu, L. Zhang, T. Li, T. Qian

School of Chemistry and Chemical Engineering, Nantong University, Nantong 226019, China.

E-mail: lfzhang@ntu.edu.cn (L. Zhang); litongfei@ntu.edu.cn (T. Li)

C. Yan

School of Petrochemical Engineering, Changzhou University, Changzhou 213164, China

Key Laboratory of Core Technology of High Specific Energy Battery and Key Materials for Petroleum and Chemical Industry, College of Energy, Soochow University, Suzhou 215006, China.

Experimental Section

Materials

The Potassium tetrachloropalladate (K_2PdCl_4, 98%, Pd>34.9%), Rhodium (III) chloride trihydrate ($RhCl_3 \cdot 3H_2O$, 99%, Rh>39%), Polyethylenimine (PEI, mW=1200) were acquired from Energy Chemical, ethanol, Nafion solution (5%), and Vulcan XC-72 carbon were purchased from Sigma-Aldrich. All chemicals were used without further purifications.

Synthesis of PdRh@PEI metallene

In the typical preparation of PdRh@PEI medium-entropy alloy, initially, dissolve K_2PdCl_4 and $RhCl_3 \cdot 3H_2O$ in DI to prepare a 40 mM solution. Then, 1 mL K_2PdCl_4 (40 mM), 1 mL $RhCl_3 \cdot 3H_2O$ (40 mM) and 4 mL DI were dissolved in a 10 ml vial. After the mixture is thoroughly mixed, add 8 mg of PEI and stir for another 20 min. Finally, the uniformly mixed sample was placed in an oil bath and reacted at 95 ^oC for 4 h. The final product was washed and collected by centrifugation with DI at 10000 rpm to obtain the PdRh@PEI metallene. For comparison, the PdRh metallene was produced under the same synthetic conditions only without adding PEI. Besides, when the molecular weight of PEI becomes 600 or 1800, while all other conditions remain unchanged, the sample were received and denoted as PdRh@PEI-600, and PdRh@PEI-1800, respectively.

Materials characterization

The surface morphologies were characterized using scanning electron microscopy (SEM Sigma 500). The transmission electron microscopy (TEM) images were collected using a JEM-2100F TEM operating at 200 kV. HAADF-STEM images and EDS mappings were taken using the Titan Themis G2 STEM at 300 kV. Atomic force microscopy (AFM) data was recorded with a Bruker Dimension ICON. Contact angle measurements were investigated using a contact drop angle measurement (JCY-1, FANGRUI). X-ray diffraction (XRD, Bruker D8) measurements were performed with Cu Kα radiation (λ=1.54056 Å). The surface chemical state analysisby XPS were performed on thermo scientific ESCALAB 250Xi with Al kα 150W. The metal content was determined by an inductively-coupled plasma mass-spectrometer (Agilent 8900x QQQ-ICP-MS, Agilent, USA).

Electrochemical measurements

All electrochemical tests in this study were performed using a three-electrode system controlled by a CHI 660E electrochemistry station (Shanghai Chenhua Instrument Corporation, China). The measurement system (conventional three-electrode cell) included a rotating disk ring electrode (RRDE, 5 mm in diameter) loaded with catalysts, a carbon rod and a calomel (saturated HgO) were used as working electrode, counter electrode and reference electrodes,

respectively, and O_2-saturated 0.1 M KOH aqueous was used as the electrolyte. The catalyst slurry was prepared by dispersing 5.0 mg of electrocatalyst in 600 μL of ethanol, 300 μL deionized and 100 μL of Nafion solution, followed by sonication for 30 minutes. Subsequently, 10 μL of the as-obtained suspension was pipetted onto the disk electrode, which was naturally dried prior to use. The loading of our Pd-based catalyst is maintained at approximately 0.5 mg cm^{-2}. Cyclic voltammetry (CV) tests were performaed using the CHI 660E electrochemistry workstation, with a potential range from 0 to 1.3 V and a scan rate of 50 mV s^{-1}. The kinetics of electrochemical oxidation of catalysts were evaluated by Linear sweep voltammetry (LSV) system at 5 mV s^{-1} with the potential range of 0.1 to 1.05 V. The rotating speed of the working electrode was 1600 rpm throughout the experiments, and all potentials were transformed to reversible hydrogen electrode (RHE).

AEMFC tests:

10 mg of PdRh@PEI was added into mixture solution containing of IPA, DI water, and Nafion to prepare the catalyst ink. The loading of our Pd-based catalyst is maintained at approximately 0.5 mg cm^{-2}. Subsequently, the as-made ink was brush painted on one side of anion exchange membrane (W-25) to form the cathode catalyst layer. Commercial 40 wt% Pt/C (Johnson Matthey) was used as an anode catalyst for forming the anode catalyst layer on the opposite side of the membrane. The catalyst-coated membranes (CCMs) with an active area of 4 cm^2 were then sandwiched between two gas diffusion layers (GDLs). The fuel cell performance was examined at 40 ^oC under humidified H_2 and air flow rates of 100 sccm at 80% relative humidity, with a back pressure of 150 kPa.

Computational Section

We utilized the VASP[1,2] software for conducting density functional theory (DFT) calculations within the generalized gradient approximation (GGA) using the Perdew-Burke-Ernzerhof (PBE)[3] formulation. The projected augmented wave (PAW) potentials[4] were selected to describe the ionic cores, while valence electrons were taken into consideration using a plane wave basis set with a kinetic energy cutoff of 450 eV. Partial occupancies of the Kohn−Sham orbitals were permitted using the Gaussian smearing method with a width of 0.05 eV. The electronic energy was deemed self-consistent when the energy change was less than 10^{-5} eV, and geometry optimization was considered convergent when the energy change was smaller than 0.05 eV/Å. Additionally, we sampled the brillouin zone with a 3 × 3 × 1 Monkhorst mesh[5]. The ORR steps:

$$* + O_2(g) + H_2O(l) + e^- \rightarrow *OOH + OH^- \quad (1)$$

$$*OOH + e^- \rightarrow *O + OH^- \quad (2)$$

$$* O + H_2O(l) + e^- \rightarrow * O \quad (3)$$

$$* OH + e^- \rightarrow * + OH^- \quad (4)$$

Gibbs free energy can be obtained by adding corrections including entopic (*TS*) and zero-point energy (ZPE) to calculated DFT energy, so that $\Delta G = \Delta E_{DFT} + \Delta ZPE - T\Delta S - eU$.

where the E_{DFT} is the calculated DFT reaction energy, ΔZPE is the change in ZPE calculated from the vibrational frequencies and ΔS is the change in the entropy referring to thermodynamics databases. The electrode potential are adopted with respect to the reversible hydrogen electrode, which makes the standard electrochemical potential of electron involved in reaction (G_e) equal to -eU, and the standard electrochemical potential of the proton (G_{H+}) equal to that of the hydrogen atom in gaseous H_2 ($1/2G_{H2}$). Considering that the triplet state of the O_2 molecule is poorly described in the current DFT scheme, the free energy of the O_2 molecule was derived according to $G_{O2} = 2G_{H2O} - 2G_{H2} + 4.92$.

The overpotential (η^{ORR}) of ORR was defined as:

$$\eta^{ORR} = \max\{\Delta G1, \Delta G2, \Delta G3, \Delta G4\}/e + 1.23 \quad (5)$$

Where the ΔG1, ΔG2, ΔG3, ΔG4 are the free energy for four elementary reactions of ORR.

Note: The idealized models inherent in conventional DFT calculations—such as perfectly ordered surfaces, zero applied potential, and the omission of solvation effects—inevitably introduce systematic inaccuracies, resulting in notable quantitative discrepancies between computed absolute energy barriers and their experimentally measured counterparts. The absolute value comparison with Pt/C is mainly used to provide background reference, and the influence of DFT system error on the absolute value in this case is inevitable.

References

[1] Kresse, G.; Furthmüller, J. Efficiency of Ab-Initio Total Energy Calculations for Metals and Semiconductors Using a Plane-Wave Basis Set. *Comput. Mater. Sci*. **1996**, 6, 15−50.

[2] Kresse, G.; Furthmüller, J. Efficient Iterative Schemes for Ab Initio Total-Energy Calculations Using a Plane-Wave Basis Set. *Phys. Rev. B* **1996**, 54, 11169−11186.

[3] Perdew, J. P.; Burke, K.; Ernzerhof, M. Generalized Gradient Approximation Made Simple. *Phys. Rev. Lett.* **1996**, 77, 3865−3868.

[4] Kresse, G.; Joubert, D. From Ultrasoft Pseudopotentials to the Projector Augmented-Wave Method. *Phys. Rev. B* **1999**, 59, 1758-1775.

[5] H. J. Monkhorst and J. D. Pack, *Phys. Rev. B*, **1976**, 13, 5188-5192.

Figures and Tables

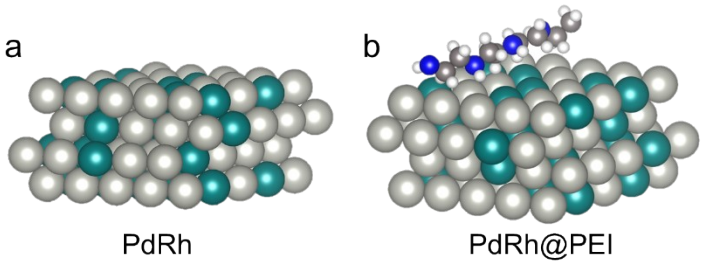

Fig. S1. Illustration of crystal structures of (a) PdRh, and (b) PdRh@PEI models. The grayish-white and dark green balls represent Pd, and Rh atoms, respectively.

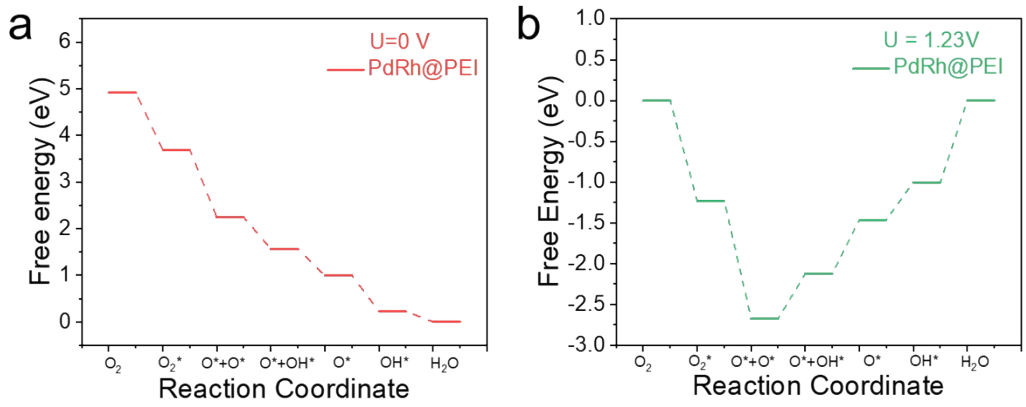

Fig. S2. Free energy plot for the ORR process on PdRh@PEI at (a) U=0 V and (b) U=1.23 V, respectively.

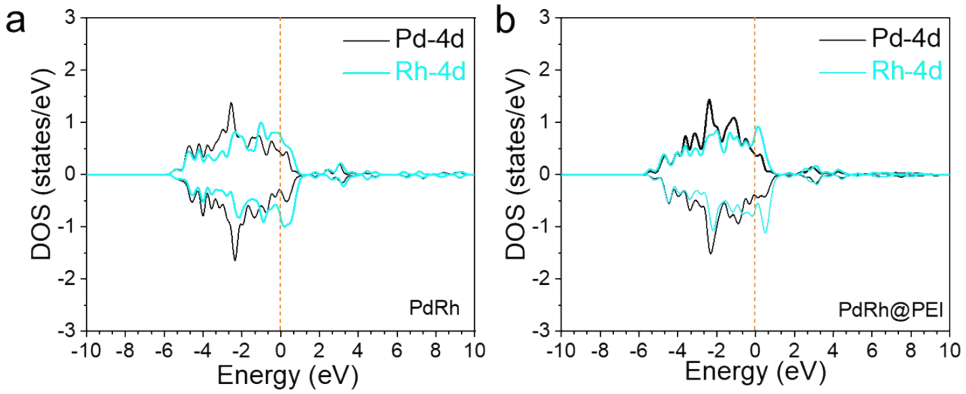

Fig. S3. PDOS spectra of Pd-4d and Rh-4d in (a) PdRh, and (b) PdRh@PEI, respectively.

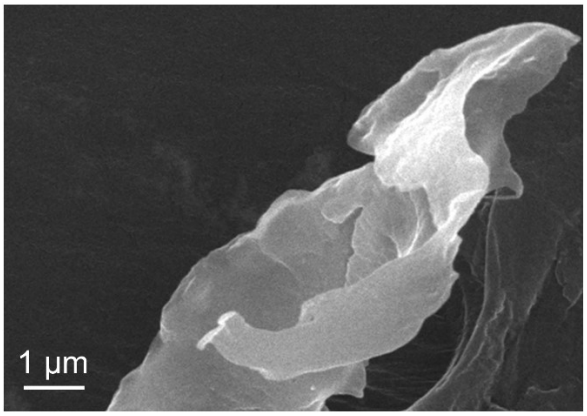

Fig. S4. SEM image of PdRh@PEI metallene.

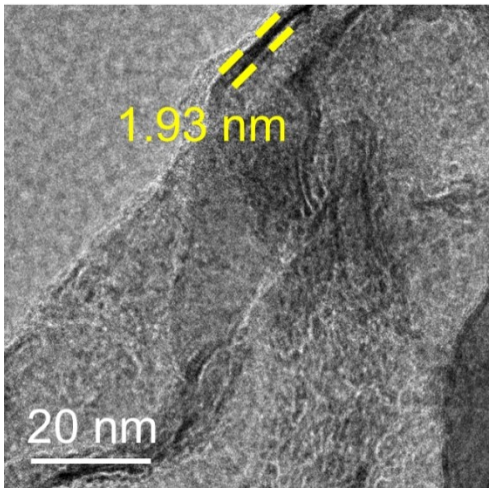

Fig. S5. TEM image of PdRh@PEI metallene.

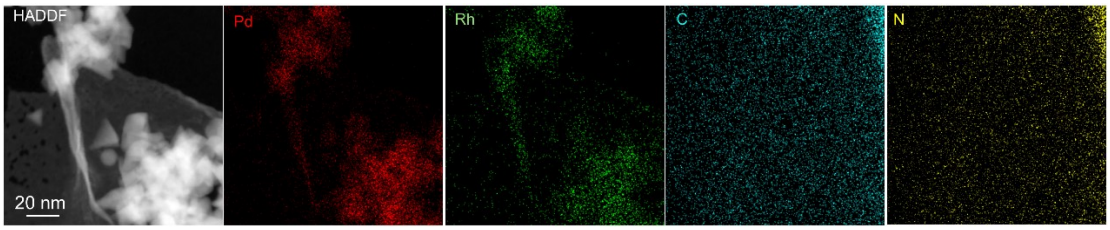

Fig. S6. HAADF and corresponding EDS elemental mapping images of PdRh@PEI metallene.

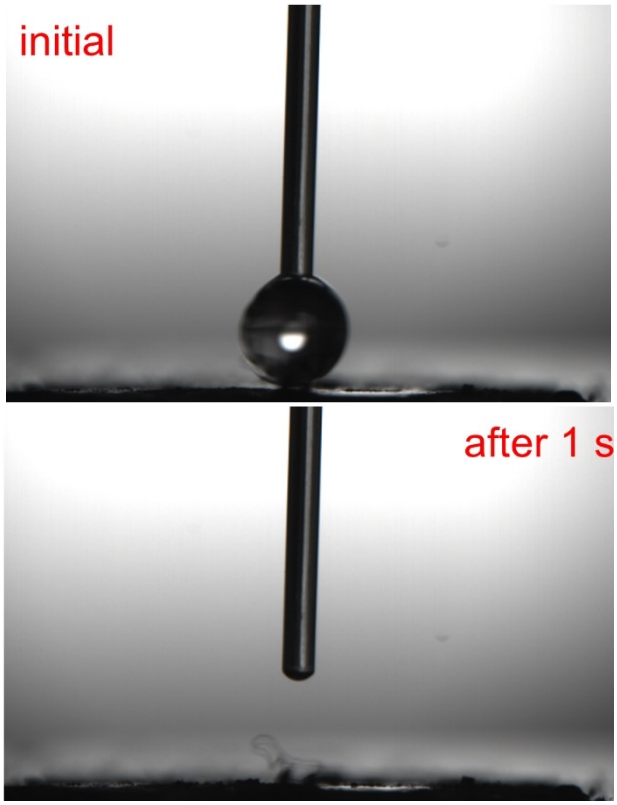

Fig. S7. Contact angle test of PdRh@PEI metallene.

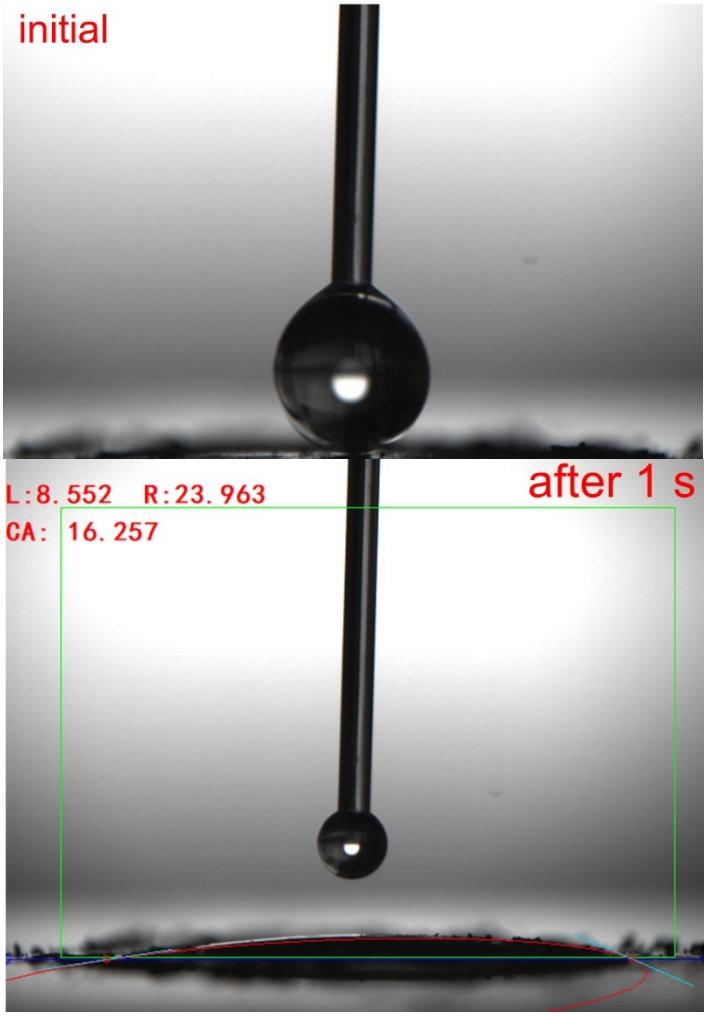

Fig. S8. Contact angle test of PdRh metallene.

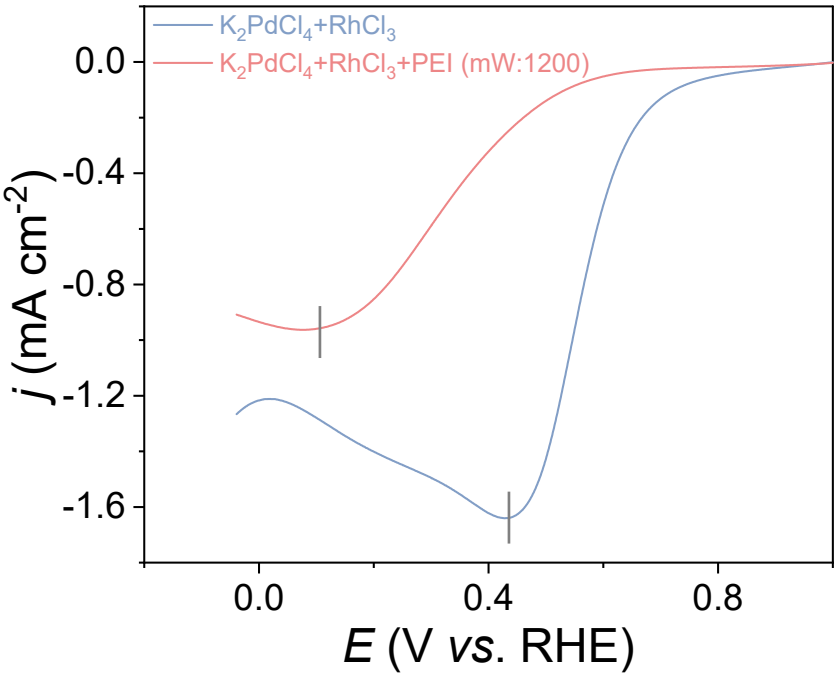

Fig. S9. LSV curves of K_2PdCl_4 + $RhCl_3$ and K_2PdCl_4 + $RhCl_3$ + PEI coated on the glassy carbon electrode at 0.1 V s^{-1} in 0.1 M KCl electrolyte.

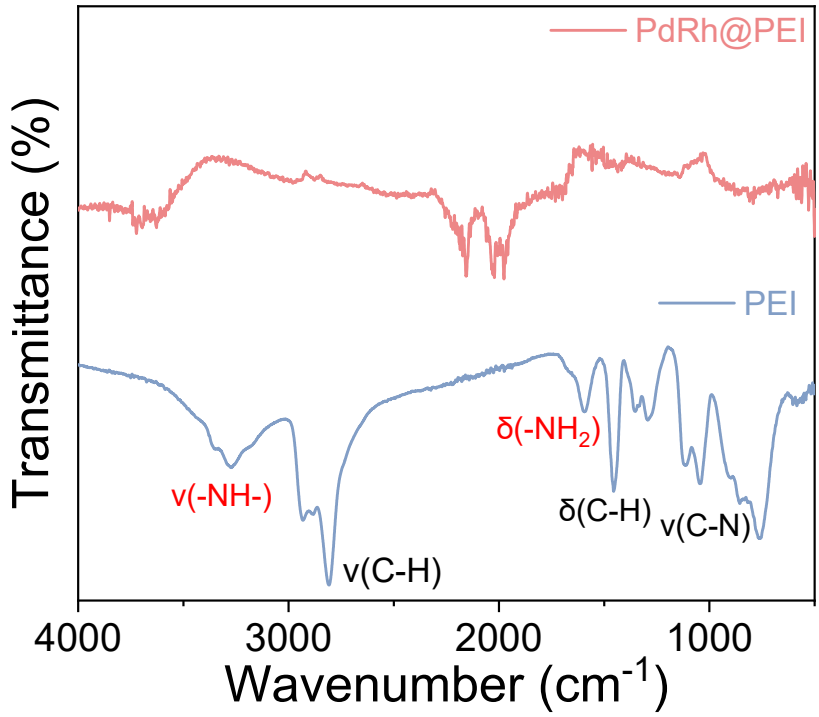

Fig. S10. FTIR spectrum of PdRh@PEI metallene.

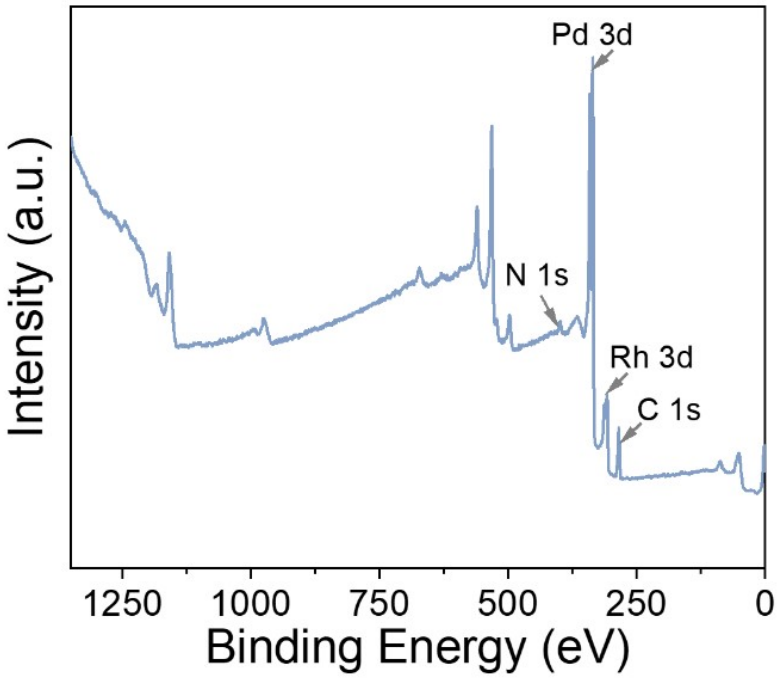

Fig. S11. XPS survey spectrum of PdRh@PEI metallene.

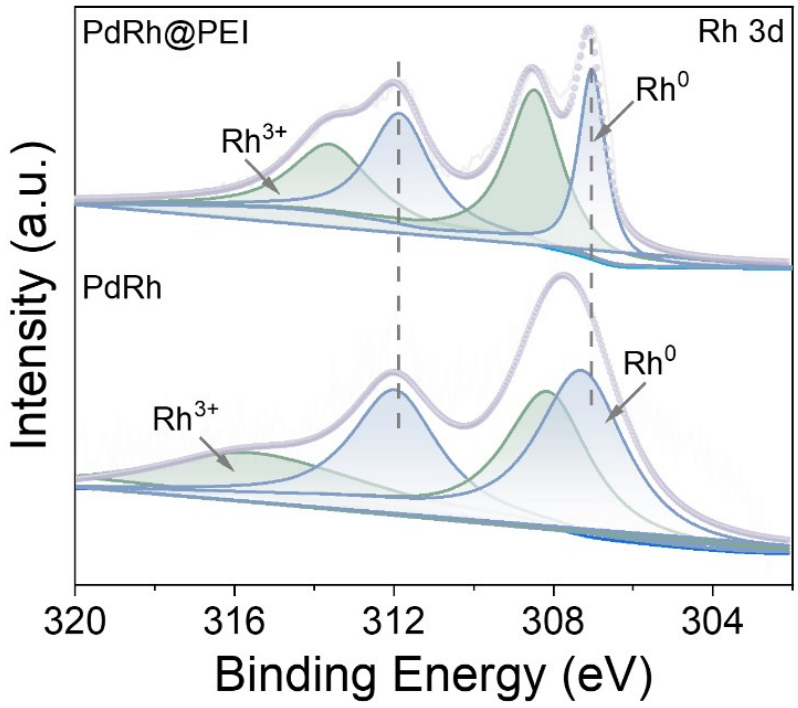

Fig. S12. XPS spectra of Rh 3d region.

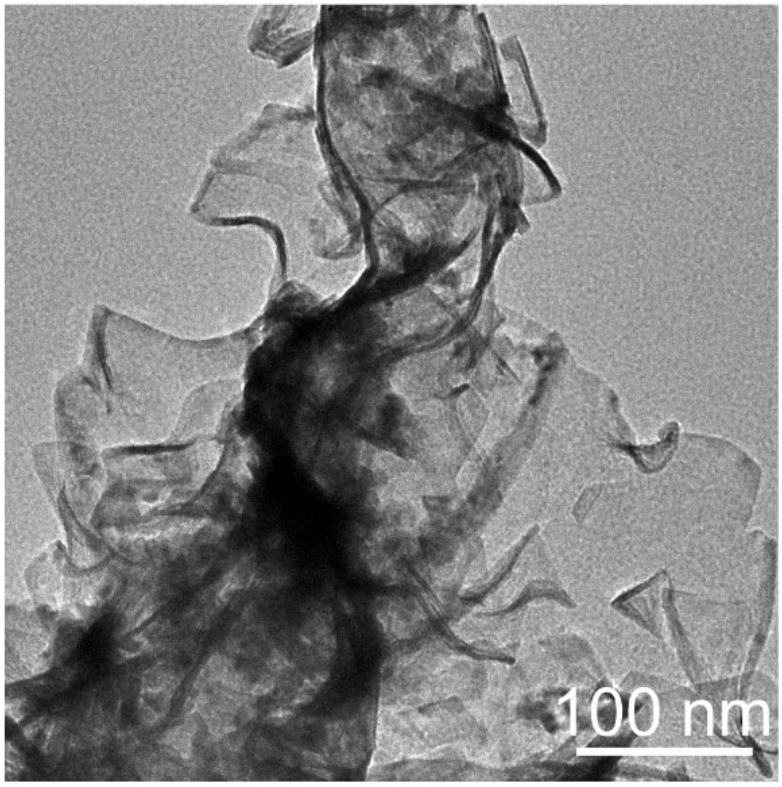

Fig. S13. TEM image of PdRh metallene.

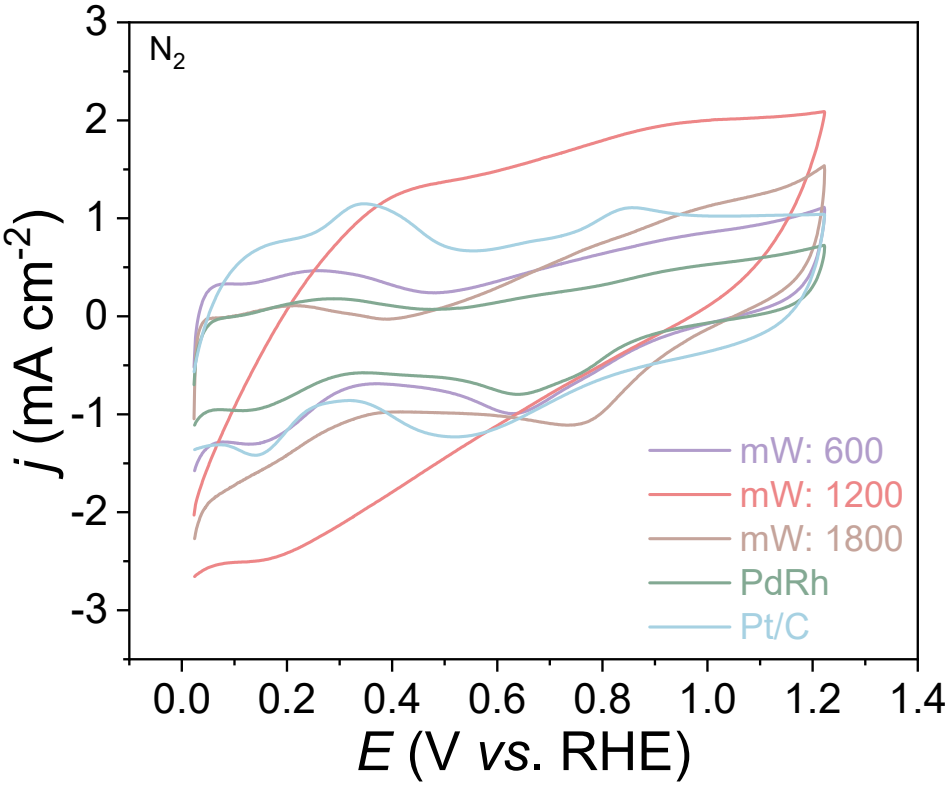

Fig. S14. CV curves of different samples under N_2-saturated 0.1 M KOH electrolytes.

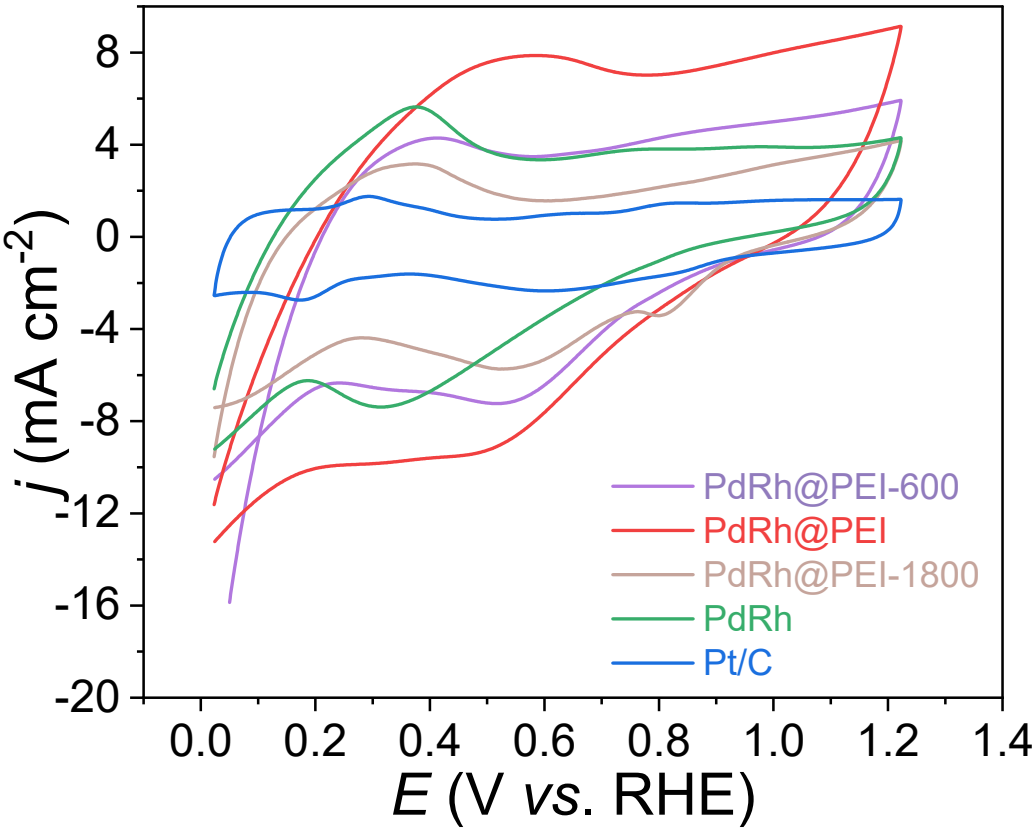

Fig. S15. CV curves of different samples under O_2-saturated 0.1 M KOH electrolytes.

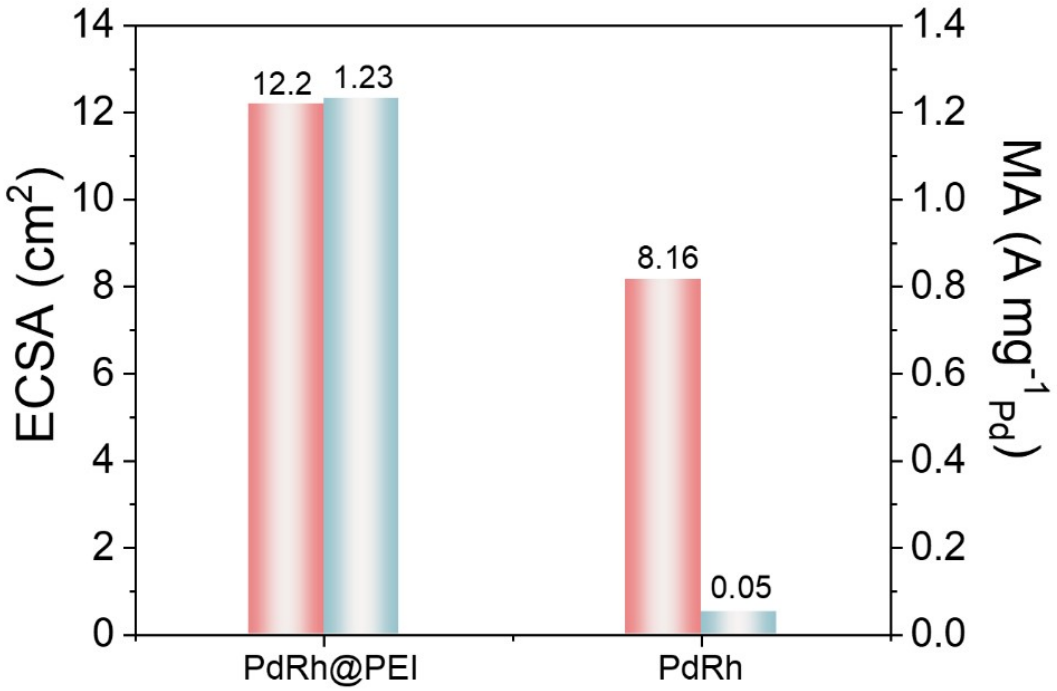

Fig. S16. Statistics for ECSA and MA values.

.

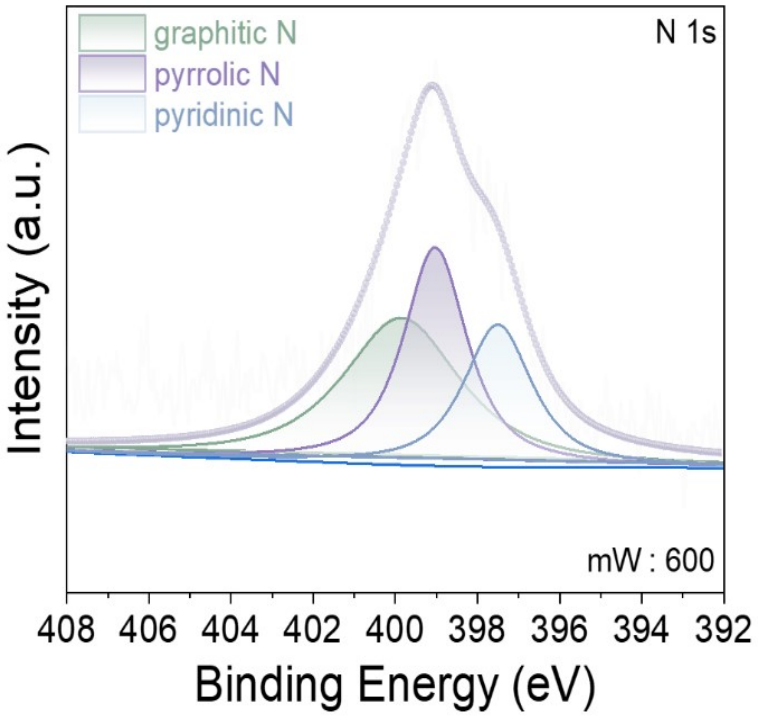

Fig. S17. XPS spectra of N 1s region of PdRh@PEI-600.

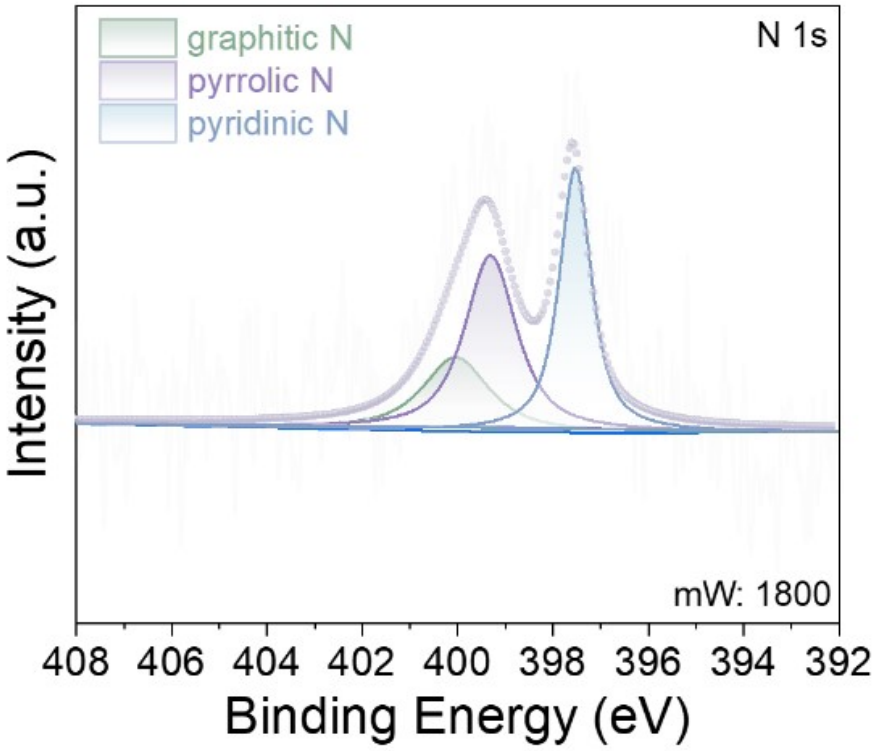

Fig. S18. XPS spectra of N 1s region of PdRh@PEI-1800.

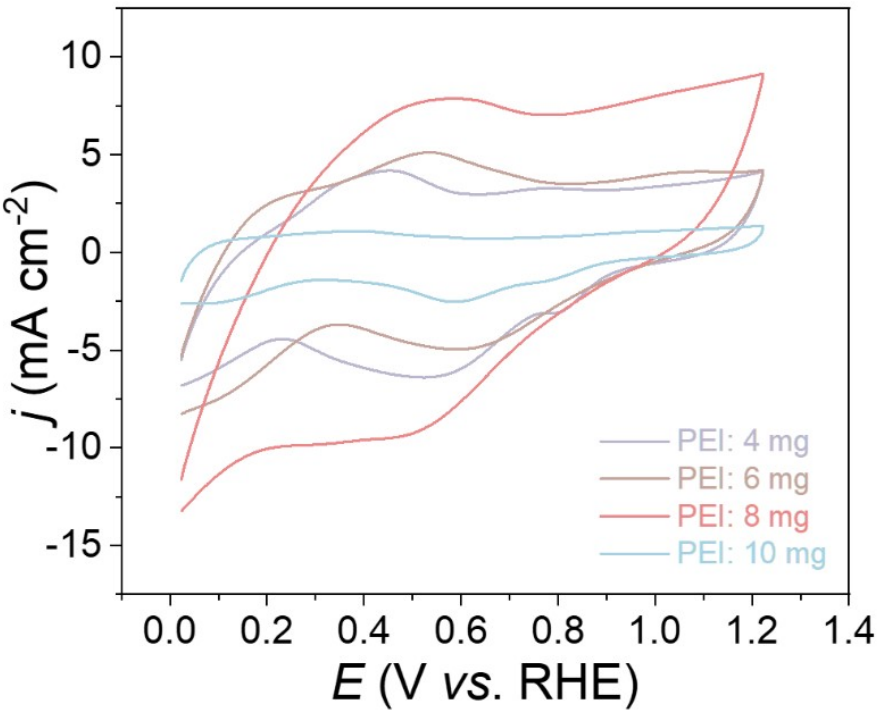

Fig. S19. CV curves under O_2 electrolytes of different dosage of PEI (mW: 1200).

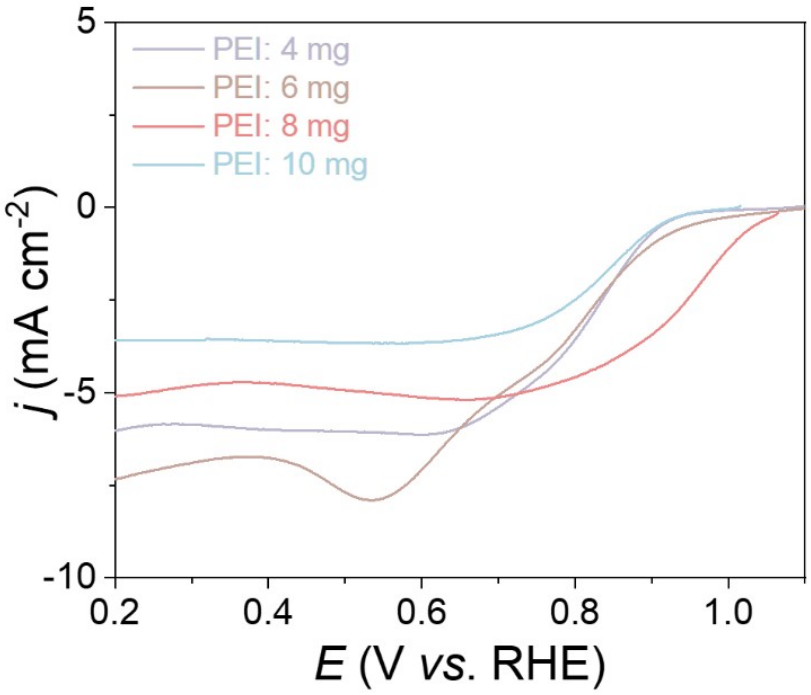

Fig. S20. LSV curves under O_2 electrolytes of different dosage of PEI (mW: 1200).

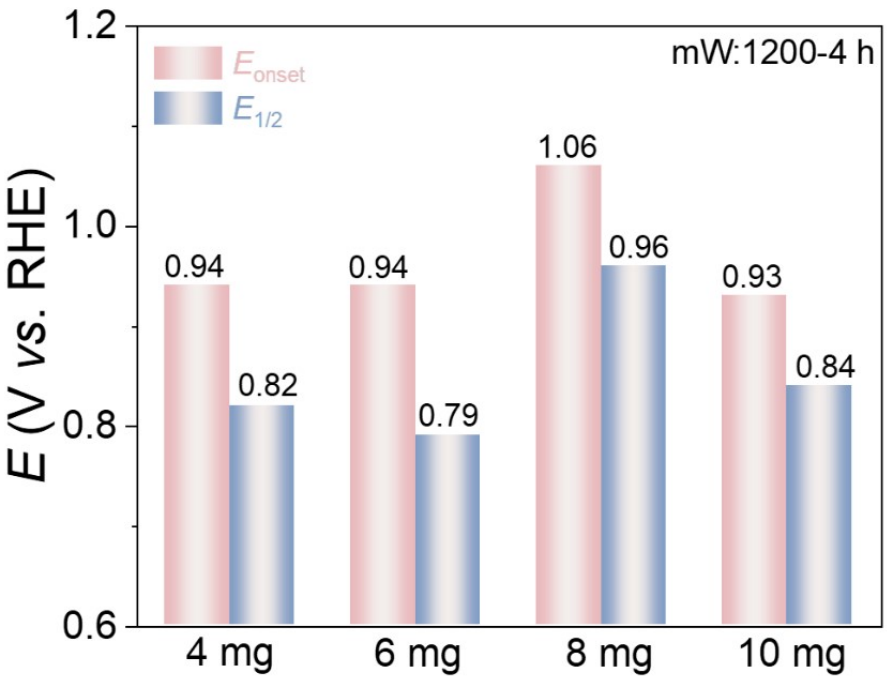

Fig. S21. Statistics for E_0, $E_{1/2}$ of different dosage of PEI (mW: 1200).

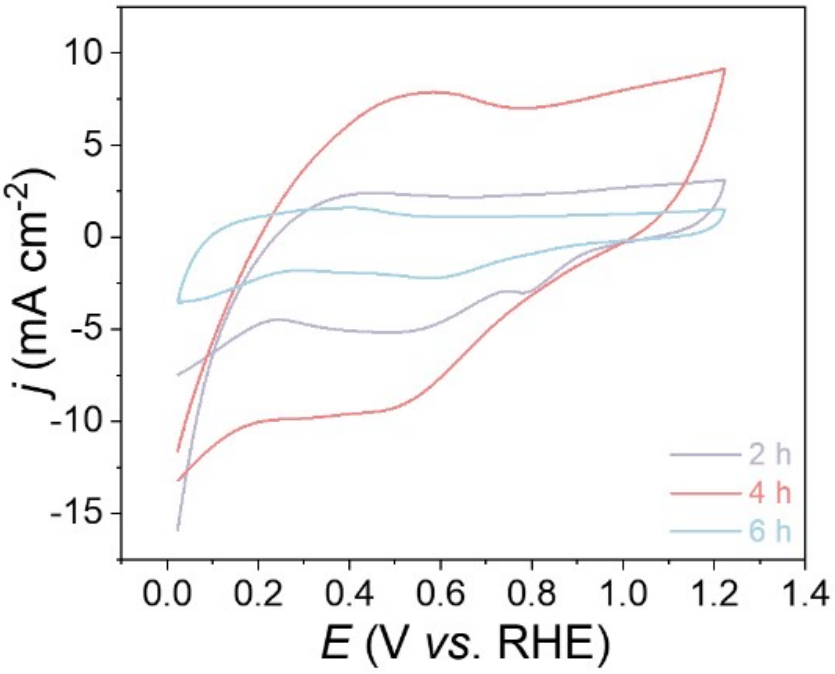

Fig. S22. CV curves under O_2 electrolytes of different reaction time.

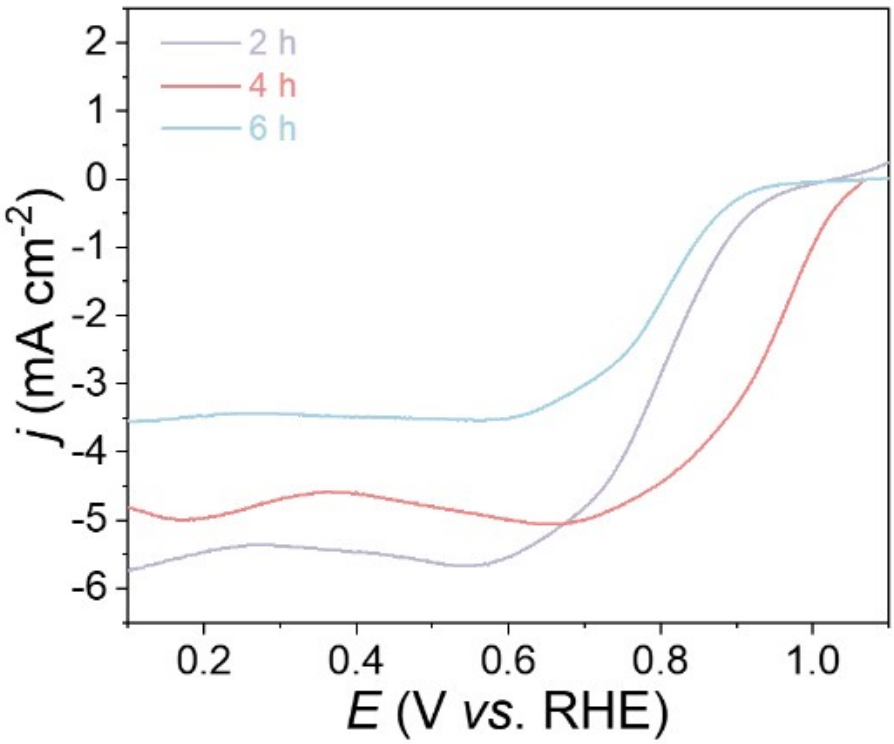

Fig. S23. LSV curves under O_2 electrolytes of different reaction times.

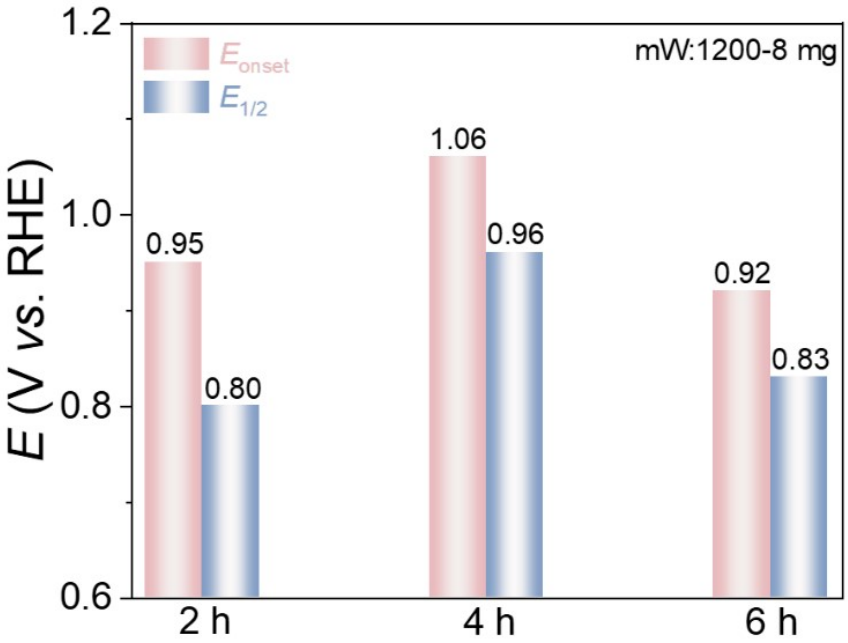

Fig. S24. Statistics for E_0, $E_{1/2}$ of different reaction time.

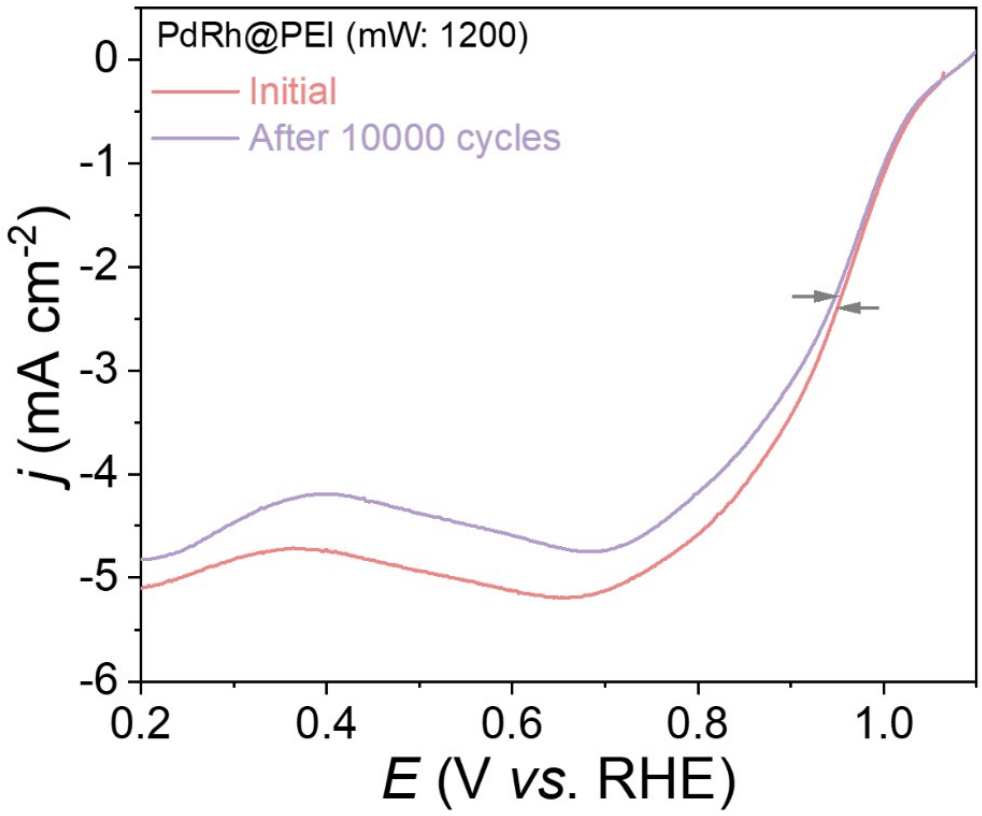

Fig. S25. LSV curves before and after ADT of PdRh@PEI.

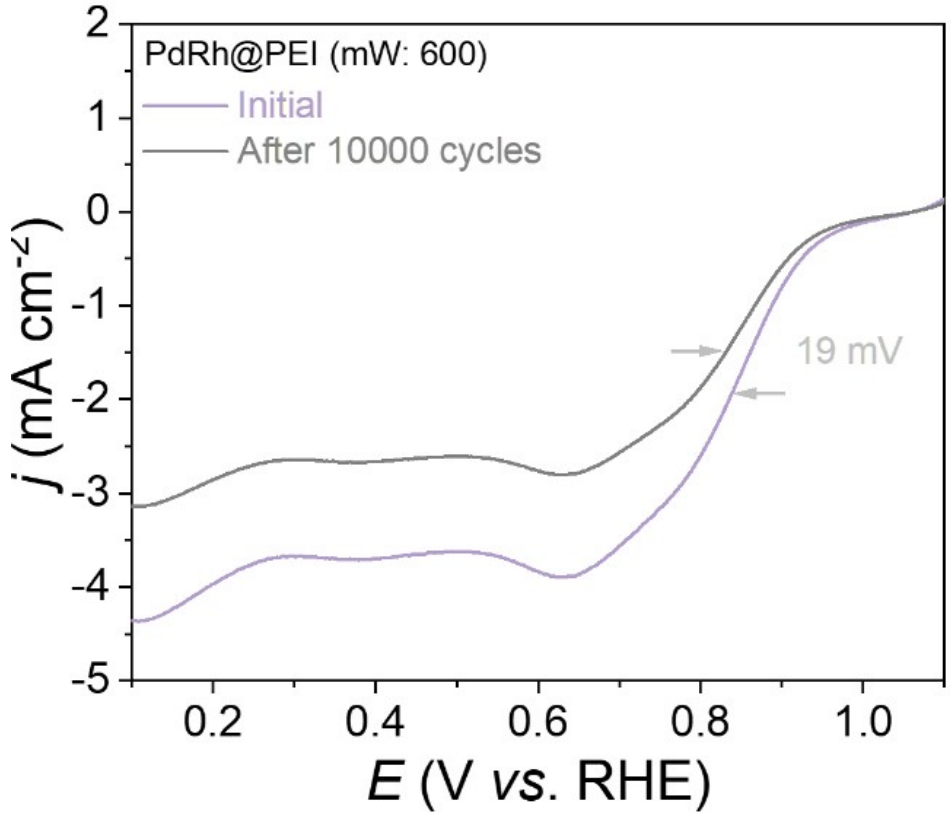

Fig. S26. LSV curves before and after ADT of PdRh@PEI-600.

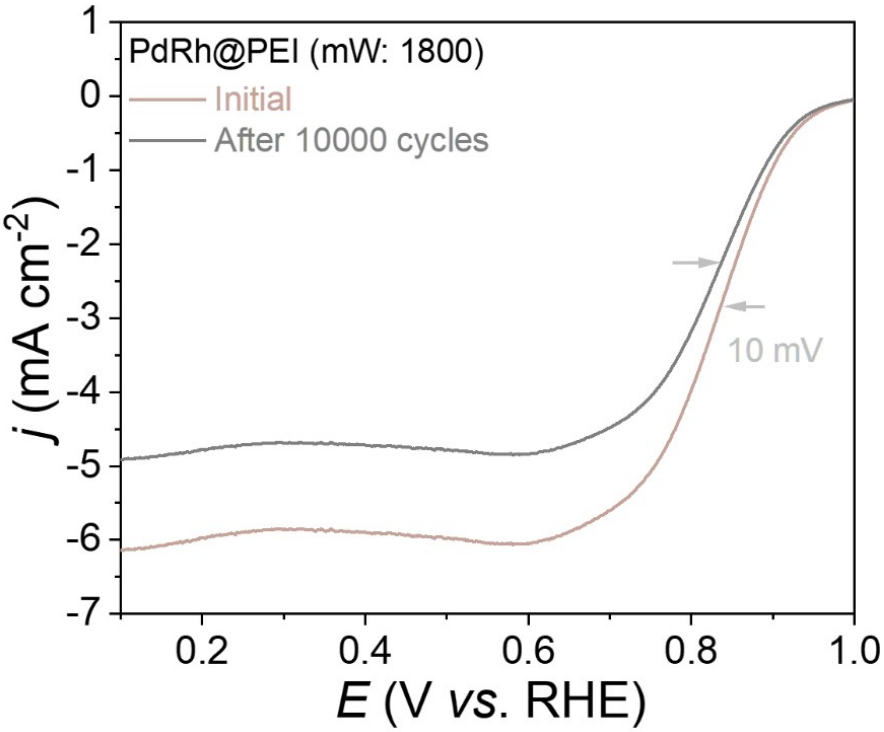

Fig. S27. LSV curves before and after ADT of PdRh@PEI-1800.

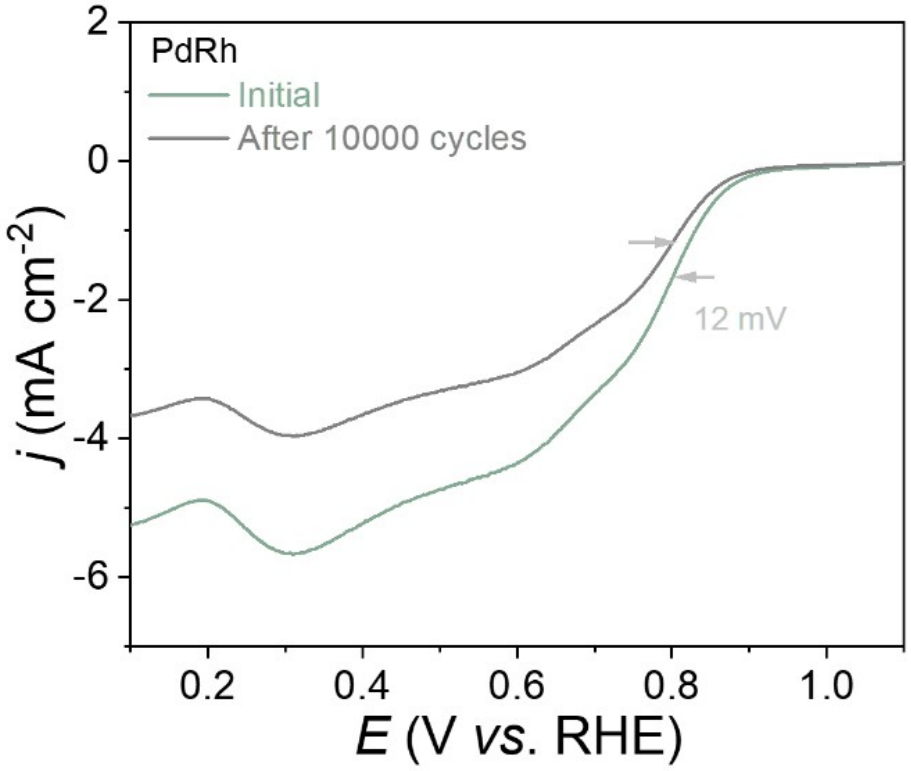

Fig. S28. LSV curves before and after ADT of PdRh.

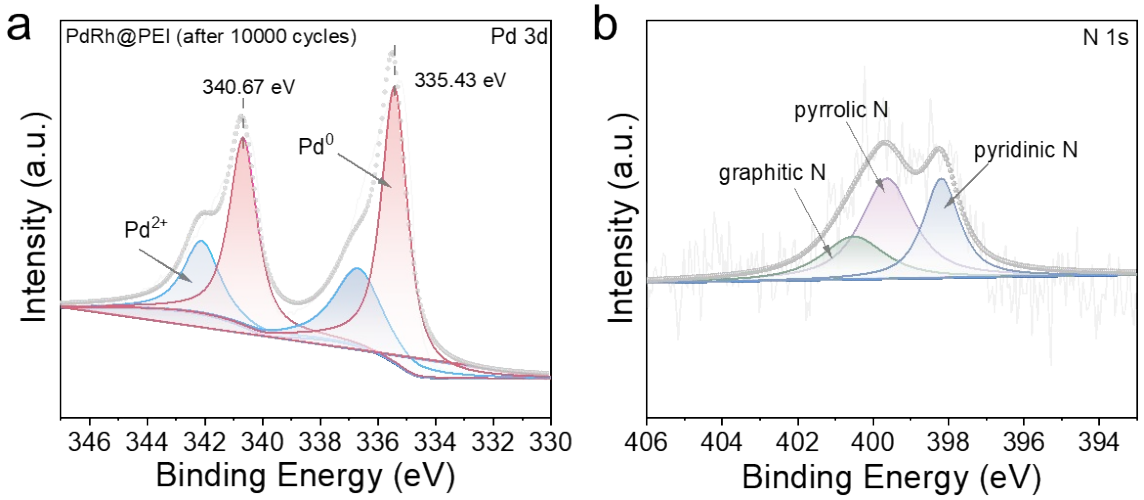

Fig. S29. XPS spectra of PdRh@PEI after 10000 cycles. (a) Pd 3d region, and (b) N 1s region.

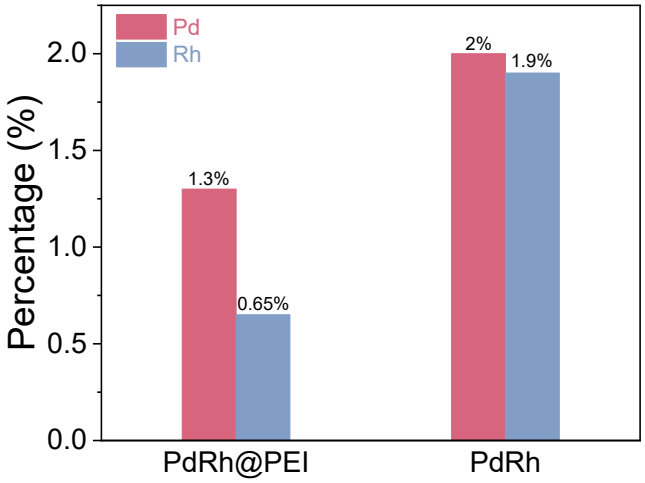

Fig. S30. The percentage content of dissolved PdRh metal was measured via ICP-OES after 10000 cycles of testing.

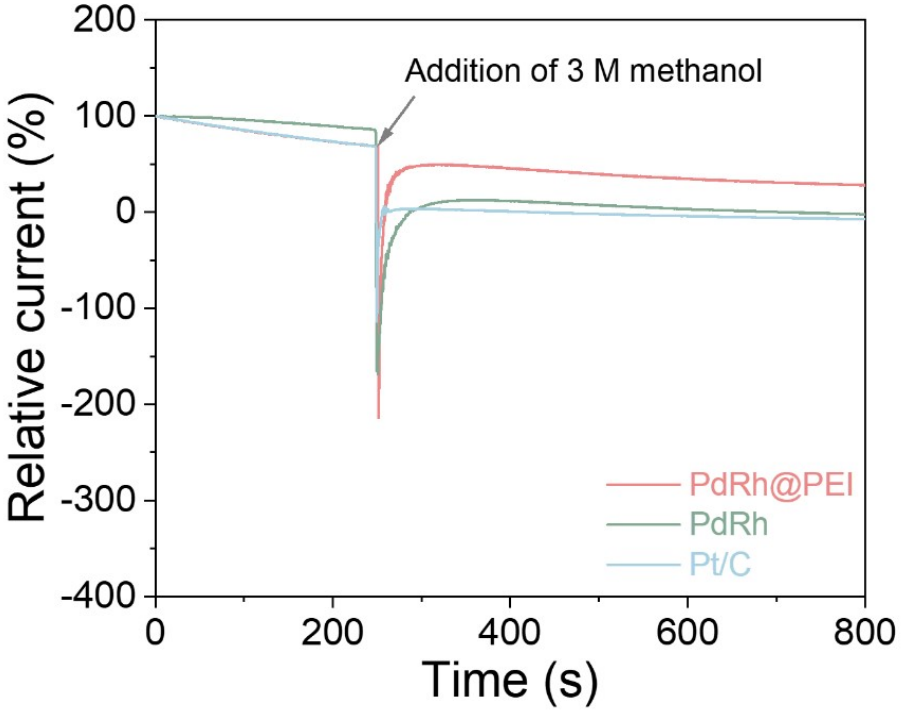

Fig. S31. Methanol resistance measurement.

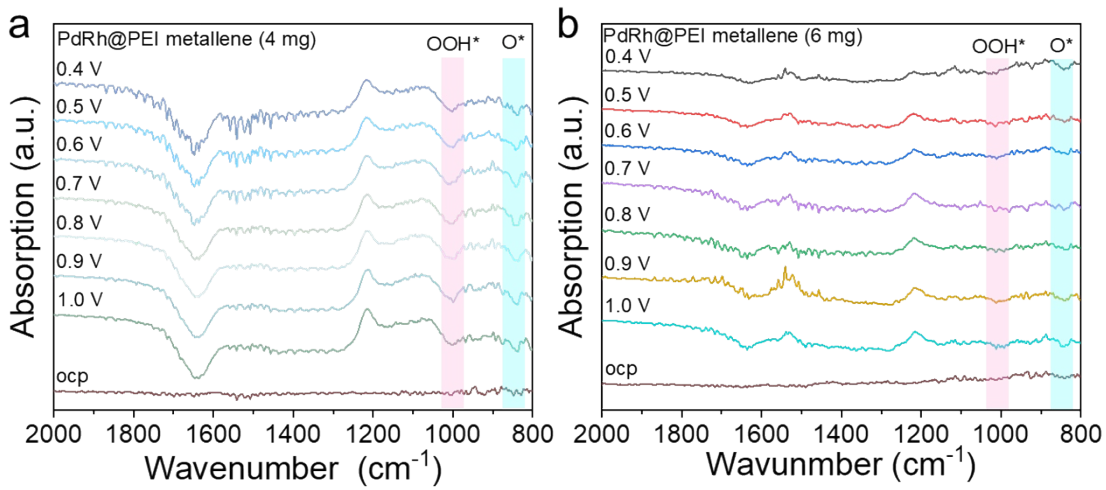

Fig. S32. (a) In situ ATR-FTIR spectra of PdRh@PEI metallene (4 mg) and (b) PdRh@PEI metallene (6 mg) recorded in an O_2-saturated 0.1 M KOH solution during the ORR process.

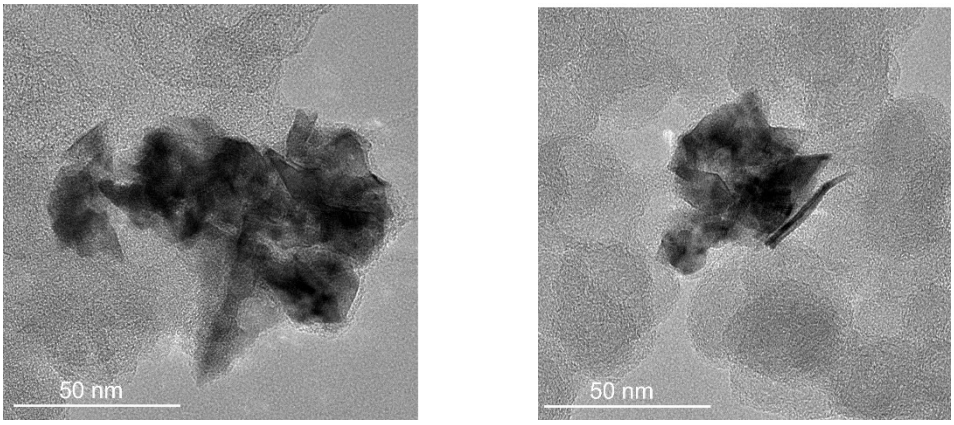

Fig. S33. TEM images of PdRh@PEI after AEMFC test.

Tabel S1. ICP results of PdRh@PEI metallene.

Element	wt%
Pd	65.03
Rh	17.58

Table S2. The comparison of E_0 and $E_{1/2}$ of PdRh@PEI metallene with those of reported

advanced materials in alkaline media.

	Catalyst	E_{onset}/V	$E_{1/2}$/V	Electrolyte	Ref
1	PdRh@PEI	1.06	0.96	0.1 M KOH	This work
2	$PdPbH_x$	--	0.958	0.1 M KOH	Nat. Commun., 2025, 16, 5262
3	Pd-Gd_2O_3	0.986	0.877	0.1 M KOH	Angew. Chem. Int. Ed., 2023, 62, e202314565
4	M-Pd/C NS	--	0.927	0.1 M KOH	Angew. Chem. Int. Ed., 2024, 63, e202407658
5	c/a-Pd@PdRh NSs/C	--	0.954	0.1 M KOH	Adv. Mater., 2024, 36, 2314252
6	Pd_2RuOx	0.980	0.890	0.1 M KOH	Adv. Mater., 2023, 35, 2208860
7	Pd/Co@N-C	--	0.88	0.1 M KOH	Nat. Commun., 2023, 14, 1346
8	Pd MoO_3/C (40%)	--	0.84	0.1 M KOH	Rare Met., 2023, 42, 1516–1525
9	$Pd_{92}Pt_8H_{41}$ NWs/C	--	0.942	0.1 M KOH	Nat. Catal., 2024, 7, 719-732
10	5-Pd-HECs/C	--	0.902	0.1 M KOH	Chem. Commun., 2024, 60, 3591–3594

Table S3. The comparison of MA of PdRh@PEI metallene in alkaline media.

	Catalyst	MA	Electrolyte	Ref
1	PdRh@PEI	1.233	0.1 M KOH	This work
2	$Pt_{37}Cu_{56}Au_7$	0.871	0.1 M KOH	ACS Catal., 2020, 10, 9967–9976
3	Ru_1/N-C_{Pores}	0.31	0.1 M KOH	Adv. Sci., 2025, 12, 2410784
4	$Pd_{17}Se_{15}$	0.206	0.1 M KOH	Adv. Funct. Mater., 2024, 34, 2405945
5	Pd_2N	0.83	0.1 M KOH	J. Mater. Chem. A, 2021, 9, 6196–6204
6	Au-O-PdZn/C	0.105	0.1 M KOH	ACS Nano, 2019, 13, 5968−5974
7	$Pd_{17}Se_{15}$NPs/C	0.460	0.1 M KOH	Nano Lett., 2021, 21, 9, 3805–3812
8	$Pt_{37}Cu_{56}Au_7$	0.871	0.1 M KOH	ACS Catal., 2020, 10, 9967−9976
9	$Pt_{23}Cu_{52}Au_{25}$	0.311	0.1 M KOH	ACS Catal., 2020, 10, 9967−9976
10	PtNi(1:1)/KB	0.74	0.1 M KOH	ACS Appl. Nano Mater., 2022, 5, 8243−8250